Research paper

Dynamic large strain characterization of tantalum using shear-compression and shear-tension testing

A. Dorogoy*, D. Rittel

Technion –Faculty of Mechanical Engineering, Technion, Haifa, 32000, Israel

ABSTRACT

The dynamic large strain behavior of polycrystalline tantalum has been characterized using shear-compression and shear-tension experiments over a wide range of high strain rates (10^3–10^4 1/s). Tests were carried out using the recently modified shear compression specimen (SCS) on a split Hopkinson pressure bar. For shear compression, very large plastic strains of more than 5.0 were reached, in comparison with the previously reported 0.4–0.6 for cylindrical and regular SCS specimens. The large strains, which combine effects of strain rate and temperature, allow separation of these effects using the Johnson-Cook material model without performing tests at different environmental temperatures.

The dynamic shear-tension tests reached plastic strains of 2.5 at fracture, but the material's ability to sustain load in shear–tension, at a triaxiality of 0.67, starts to degrade early from plastic strain levels of 0.15. For larger plastic strains, the slope of the stress-strain curve becomes negative due to damage evolution combined with strain rate and temperature effects.

Our results indicate that the material dynamic failure behavior at high strain rates in shear-tension is markedly different from that in shear-compression, for which the rate of damage accumulation is more moderate, and hence ductility is higher.

© 2017 Elsevier Ltd. All rights reserved.

1. Introduction

Tantalum (Ta) is a ductile body-centered cubic (bcc) metal, combining a high-density and elevated melting temperature, excellent formability, good heat conductivity, good fracture toughness, corrosion resistance, and weldability (Chen and Gray, 1996). Those properties make it an attractive material for applications involving high strain rates at which a large ductility to failure is required. The mechanical properties of Ta have been extensively investigated (Bhattacharyya and Rittel, 2007; Chen and Gray, 1996; Hoge and Mukherjee, 1977; Khan and Liang, 1999; Lee et al., 1997; Nemat-Nasser and Isaacs, 1997; Rittel et al., 2009, 2007, 2002; Wei et al., 2003)], and it has been found to exhibit a high temperature and strain-rate sensitivity. Most of the dynamic available experimental results were obtained by using split Hopkinson pressure bars (Bhattacharyya and Rittel, 2007; Chen and Gray, 1996; Hoge and Mukherjee, 1977; Khan and Liang, 1999; Lee et al., 1997; Nemat-Nasser and Isaacs, 1997; Rittel et al., 2009, 2007; Wei et al., 2003). Dynamic compression tests of cylinders (Chen and Gray, 1996; Hoge and Mukherjee, 1977; Khan and Liang, 1999; Lee et al., 1997; Nemat-Nasser and Isaacs, 1997; Rittel et al., 2009, 2007)

or rectangular specimens (Wei et al., 2003) were conducted. Other tests were done under shear-compression load (Bhattacharyya and Rittel, 2007; Rittel et al., 2009) using the shear-compression specimen (SCS) (Rittel et al., 2002) or pressure-shear plate impact experiments (Duprey et al., 1998). The dynamic compression tests, using cylinders, parallelepiped or SCS specimens, were all limited by maximum attainable plastic strain of the order of 0.6. Dynamic tension or dynamic shear- tension results are more scare, and are also limited to a maximum plastic strain value of 0.3 (LeBlanc and Lassila, 1993; Pan et al., 2008).

In this work the recently modified SCS specimen, (Dorogoy et al., 2015) and the newly developed shear-tension (STS) specimen (Dorogoy et al., 2016) were utilized to investigate the tantalum large strain behavior . This investigation broadens the knowledge on tantalum stress-strain behavior. The tantalum is characterized at higher strain rates (10^4 1/s) and very large strains (higher than 5) and the contribution of temperature, strain rate and damage is separated and quantified. This investigation is also broadening the knowledge of tantalum large strain behavior under different loading conditions. The shear-compression specimen creates within the material negative triaxiality and positive Lode parameter while the shear tension specimen creates positive triaxiality and negative Lode parameter. These two parameters are known to influence the flow behavior and ductility of materials (Bai and Wierzbicki, 2008;
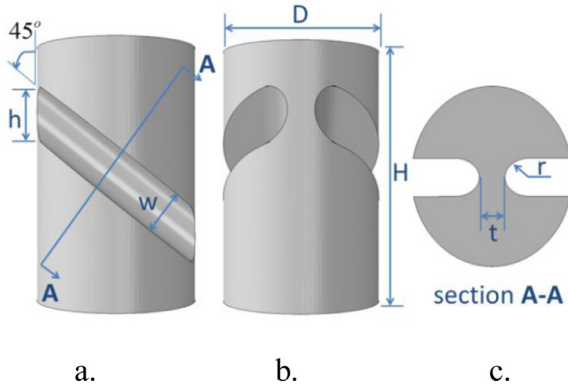
Fig. 1. An SCS specimen with a circular gauge. a. Front view b. Side view. c. A cut view (A-A) perpendicular to the gauge inclination.

Barsoum and Faleskog, 2007a; 2007b; Gao et al., 2009; Keshavarz et al., 2014; Pivonka and Willam, 2003).

Using the modified SCS in a split Hopkinson pressure bar (SHPB) (Kolsky, 1949) with the data reduction formulas, enables characterization of the stress-strain behavior of Ta up to equivalent plastic strain of 1.2 at strain rates ranging from 10^3 to 10^4 1/s. This large plastic strain causes a significant temperature rise, and reduction of strain rate, which are responsible for the observed softening. Using the Johnson-Cook (JC) material model (Johnson and Cook, 1983), these effects were separated without the need to perform tests at different environmental temperatures (Dorogoy and Rittel, 2009). By adding damage evolution to the JC model of Ta, its ductile failure behavior could further be characterized up to very high equivalent plastic strain (more than 5).

Using the STS with a split Hopkinson tension bar (SHTB) (Nicholas, 1981), the stress-strain behavior of the Ta is characterized at strain rates ranging from 10^3 to 10^4 1/s. With the aid of JC model and ductile failure with damage evolution, the stress-strain behavior is characterized up to equivalent plastic strain of 2.5 at which fracture occurs.

The second section, following the introductory section, presents the experimental results obtained with the SCS and their data reduction. The third section presents the experimental results obtained with the STS. The fourth section discusses the results presented earlier, followed by concluding remarks.

2. Dynamic properties of tantalum in shear–compression

2.1. Experimental results

Six modified SCS with a circular gauge (Dorogoy et al., 2015) were tested in a SHPB apparatus with 12.7 mm diameter hardened C300 maraging steel bars. The dimensions of the specimens are shown in Fig. 1. In this investigation: $D = 10$ mm, $H = 20$ mm, $w = 3$ mm, $r = 1.5$ mm, $t = 1.6$ mm, $h = w / \cos(\theta)$ and $\theta = 45°$.

The specimens were manufactured from an annealed (99.99%) tantalum rod Ø20 x 1500 [mm] (supplied by Ningxia Orient Tantalum Industry Co. Ltd , China) according to ASTM B365-98 RO5200 specifications. Its yield strength, tensile strength and elongation are: 238 MPa, 287 MPa and 55%, respectively. The rod composition is detailed in Table 1.

A schematic representation of the SHPB apparatus is shown in Fig. 2 with an SCS specimen. The measured interfacial incident and transmitted forces and displacements are marked with subscripts *in* and *out*, respectively. The experimental load displacement results, f_{out}-Δu for six specimens, are shown in Fig. 3 where $\Delta u = u_{in} - u_{out}$. The results in Fig. 3 are not filtered and therefore

Table 1
Composition of the tantalum rod (ppm).

Fe	Si	Mo	W	O	N
<0.005	1.4	0.92	6.5	30	27
H	**C**	**Ni**	**Nb**	**Ti**	**Ta**
2	8	< 0.005	5.3	<0.0005	Bal.

Table 2
Parameters for data reduction.

k_{31}	k_{32}	k_{33}	p_1	p_2	p_3	p_4	p_5
4.35	−5.886	3.47	0.9133	−0.2676	0.2337	−0.195	0.04498

one should consider the average curve that is insensitive to fluctuations, as representative of the material behavior.

2.2. Determination of the tantalum properties

The determination of the dynamic properties of the Tantalum in shear compression loading was done in four steps:

(1) Developing data reduction technique.
(2) Application of the data reduction technique.
(3) Determination of the strain rate and temperature effects using JC material model.
(4) Validation of the JC model and application of damage evolution.

2.2.1. Application of the data reduction technique

The data reduction technique is similar to that exposed in previous investigations (for example (Dorogoy et al., 2015)) and is detailed again in Appendix A for completeness .The data reduction formulas are:

$$\widehat{\varepsilon}_p = k_{31}\frac{d-d_y}{h} + k_{32}\left(\frac{d-d_y}{h}\right)^2 + k_{33}\left(\frac{d-d_y}{h}\right)^3 \qquad (1)$$

$$\widehat{\sigma} = \left(p_5\varepsilon_p^4 + p_4\varepsilon_p^3 + p_3\varepsilon_p^2 + p_2\varepsilon_p + p_1\right)\frac{P}{Dt} \qquad (2)$$

Where the parameters k_{31}, k_{32}, k_{33} and p_1, p_2, p_3, p_4, p_5 are detailed in Table 2.

Eqs. 1–2 map the experimentally measured load (P) and displacement (d) into the average equivalent plastic strain ($\widehat{\varepsilon}_p$) and the averaged Mises stress ($\widehat{\sigma}$) on the gauge mid cut section. This $\widehat{\sigma}$ - $\widehat{\varepsilon}_p$ have been proven to represent the material characteristic behavior (Dorogoy et al., 2015; Rittel et al., 2002). The height of the gauge is h. The geometrical parameters D and t are the diameter of the specimen and the gauge thickness. The displacement at which the gauge starts to yield (d_y) was estimated for the average curve shown in Fig. 3. The obtained averaged $\widehat{\sigma} - \widehat{\varepsilon}_p$ curve is shown in Fig. 4. An estimated (green) bi-linear curve is plotted as well. This line represent the behavior of the tantalum on the mid-cut section of the gauge. Note that the behavior is characterized up to a high plastic strain of 1.2, and it contains two regions: 1) $\widehat{\varepsilon}_p < 0.5$ with a moderate slope, and 2) $\widehat{\varepsilon}_p > 0.5$ with a significantly higher slope. This behavior will be addressed and validated numerically in the sequel.

In order to validate the prediction σ_{eq} - ε_p of Fig. 4, the experimental impact of the SCS specimen was simulated. Abaqus explicit (Simulia, 2014a) was used to perform the 3-D, dynamic and adiabatic simulations. Because of symmetry only half of an SCS specimen was modeled. The bottom of the specimen was assumed to be in frictional contact with a rigid plate as shown in Fig. 5. A coefficient of friction 0.1 for lubricated steel was used. The experimental $\Delta u = u_{in} - u_{out}$ was applied on the upper face of the SCS.
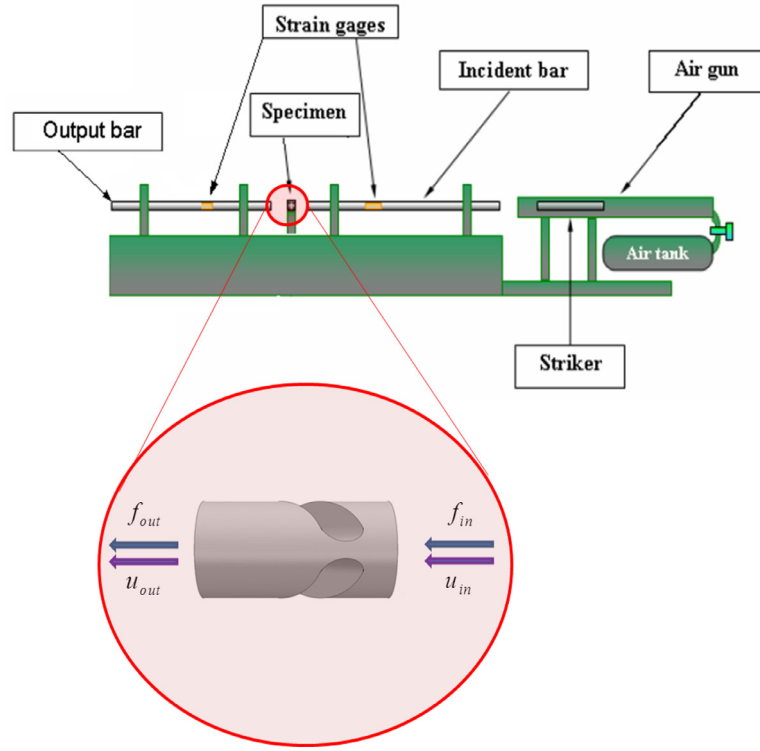
Fig. 2. Schematic representation of a SHPB apparatus showing the specimen orientation with the location of the measured quantities f_{in}, f_{out}, u_{in} and u_{out} on the specimen faces.
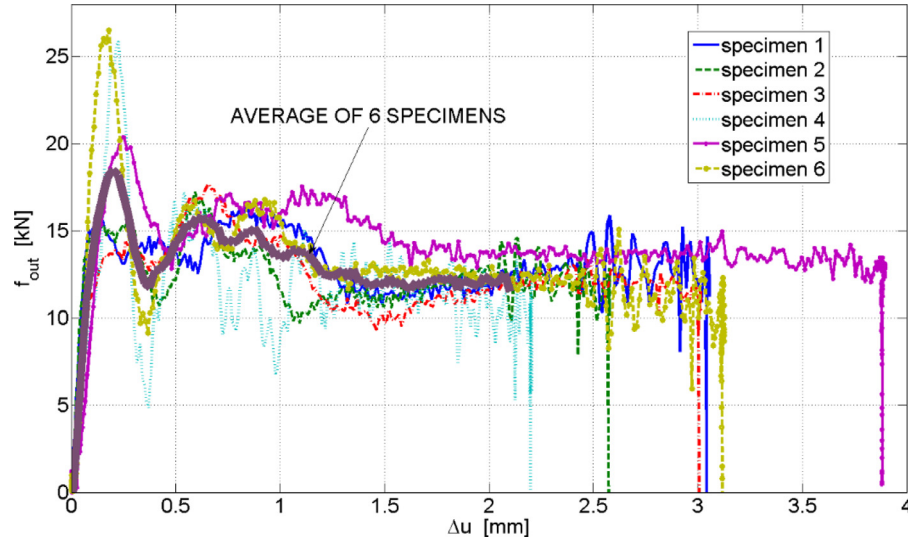

Fig. 3. Dynamic experimental results, Δu-f_{out}, of six SCS specimens made of Tantalum. Note the average curve of the 6 tests.

The purpose of this validation was to check if the experimental results $\Delta u - f_{out}$ can be replicated with the use of the measured σ_{eq} - ε_p of Fig. 4, and eventually update it until it does so. The verified σ_{eq} - ε_p input curve to Abaqus is shown in Fig 6a. It is the curve in Fig. 4 with an extension. Extension is needed because the curve of Fig. 4 was obtained under the assumption of average equivalent plastic strain, while in reality particular elements within the gauge do experience higher strains.

The resulting numerical $\Delta u - f_{out}$ in comparison to the averaged (of 6 specimens) experimental one is shown in Fig. 6b. A good

agreement can be observed. This good agreement implies that the input to Abaqus, shown in Fig. 6a, really represents the σ_{eq} - ε_p at each individual element of tantalum during the impact.

The average values of the equivalent plastic strain and Mises stress on the mid cut section of the gauge for the validated σ_{eq} - ε_p are calculated. These average values are plotted (blue line) as well in Fig. 6a. Fig. 6a therefore compares the average behavior of a single element (the input to Abaqus) to the averaged values on the mid cut section of the gauge. The comparison reveals two regions. In the region where $0 < \varepsilon_p < 0.83$ the average values do repre-
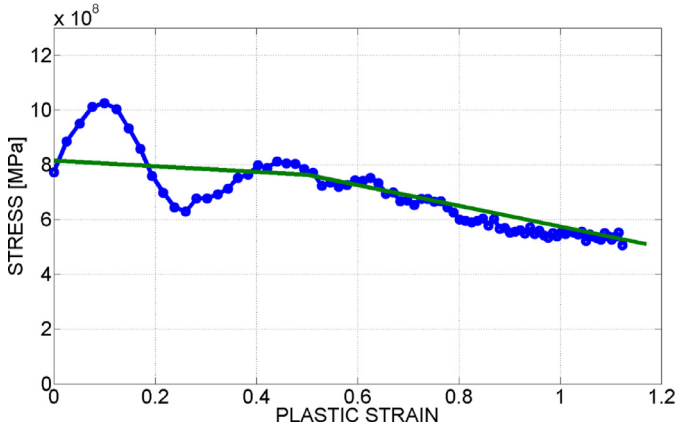
Fig. 4. The prediction of the σ_{eq} - ε_p of Tantalum using the average experimental result of Fig. 3 and the data reduction technique Eqn. (1–2). An estimated bi-linear line is plotted as well.
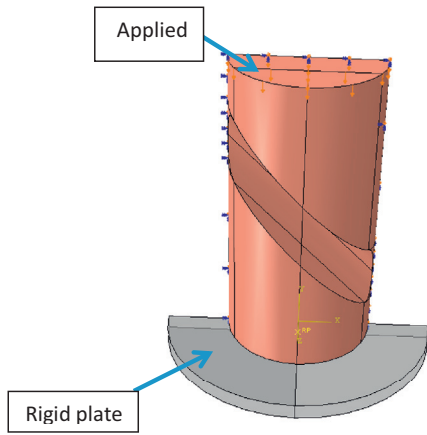
Fig. 5. The numerical model used for validation showing the geometrical model of the SCS specimen.

sent the real properties of the material but for the region where ε_p > 0.83 they diverge from the input values and hence can't be considered as representing the material property. One should bear in mind that the validated σ_{eq} - ε_p curve in Fig. 6a is neither strain-rate nor temperature dependent, while elements within the gauge experience different plastic strains, different strain rates, different temperature and damage. The validated σ_{eq} - ε_p of Fig. 6a with its
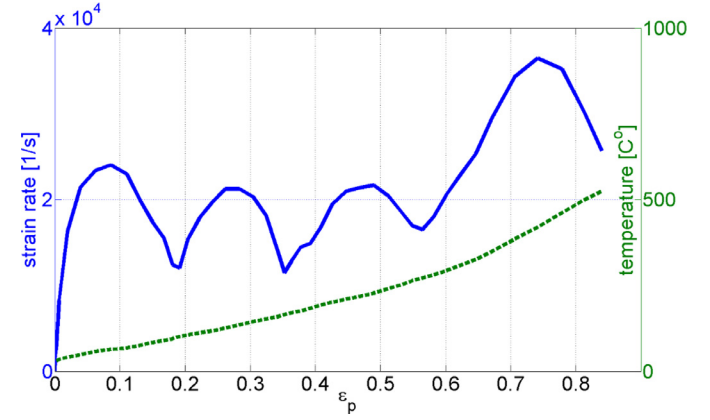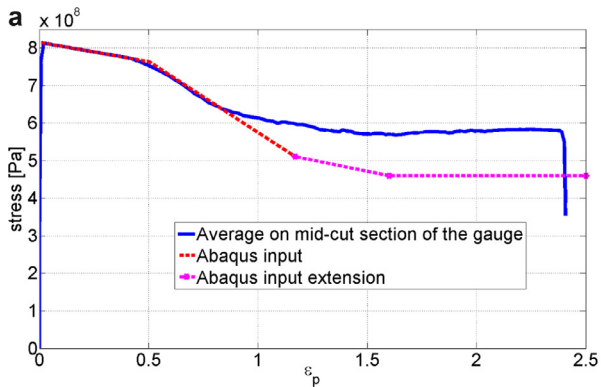
Fig. 7. The average temperature rise and strain rate on the mid cut section.

extension therefore represent a "satisfactory average" of all these effects during the impact.

The resulting numerical $\Delta u - f_{out}$ in comparison to that averaged of 6 specimens, is shown in Fig. 6b. The agreement is quite satisfactory.

Fig. 7 shows the calculated averaged strain rate and temperature on the mid cut section for the range of plastic strains over which there is agreement between the averaged plastic strain and the property of the material. It can be observed that strain rate of $\sim$ 20,000 1/s and temperature of 500 °C are readily achieved in this plastic strain region.

### 2.2.2. Determination of the strain rate and temperature effects using Johnson–Cook material model

The inelastic behavior described by Johnson-Cook (JC) (Johnson and Cook, 1983) model is used to model high strain rate deformation of metals. It is generally used in adiabatic transient dynamic analyses. The hardening is a particular type of isotropic hardening in which the flow stress σ_{eq} is assumed to be of the form:

$$\sigma_{eq} = \left[A + B(\varepsilon_p)^n\right]\left[1 + C \log\left(\frac{\dot{\varepsilon}_p}{\dot{\varepsilon}_p^r}\right)\right][1 - \Theta^m] \tag{3}$$

Where

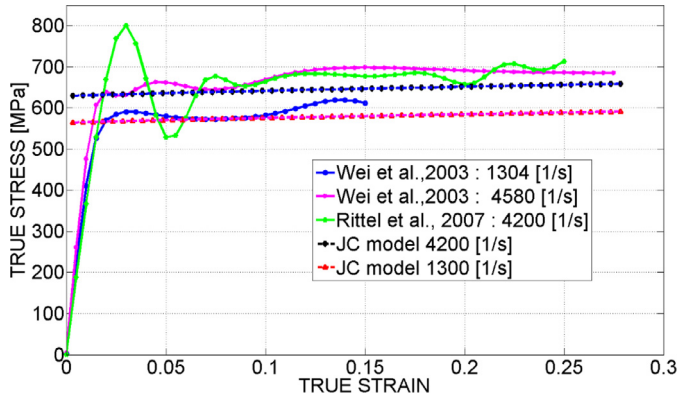$$\Theta = \begin{cases} 0 & for \quad T < T_r \\ \dfrac{T - T_r}{T_m - T_r} & for \quad T_r < T < T_m \\ 1 & for \quad T > T_m \end{cases} \tag{4}$$

In Eq. (3), ε_p is the equivalent plastic strain and A, B, C, n and m are material parameters, to be identified. The natural logarithm is
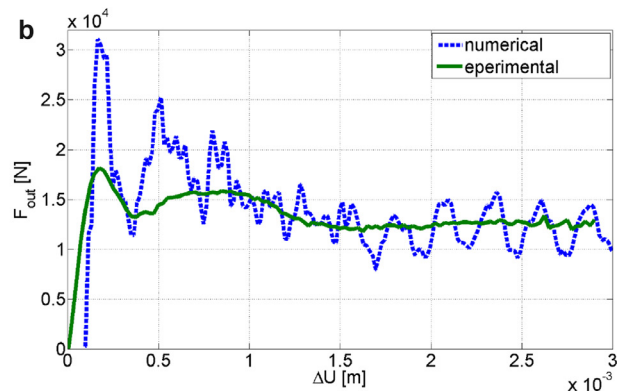
Fig. 6. a. The validated σ_{eq} - ε_p during the impact. b. The resultant numerical $\Delta u - f_{out}$ in comparison to the averaged (of 6 specimens) experimental.

Fig. 8. Dynamic stress-strain curves obtained by rectangular specimens (Wei et al., 2003) and SCS (Rittel et al., 2007) in comparison to the JC model using: A =575 MPa, B = 75 MPa, n= 0.82, C = 0.10 and $\dot{\varepsilon}_p^r = 1000$ 1/s.

Table 3
JC parameters for tantalum in shear-compression for strain rates of $10^3 - 10^4$ 1/s.

A [MPa]	B [MPa]	N	C	m	Tr [C°]	Tm [C°]	$\dot{\varepsilon}_p^r$
575	75	0.82	0.10	0.8	25	2975	1000

Table 4
Elastic and physical parameters for tantalum.

E [MPa]	ν	P	β	c_p
186	0.35	16690	1.0	138

denoted "log". Θ Is a dimensionless temperature defined in Eq. (4), where T is the current temperature, T_m is the melting temperature and T_R stands for room temperature. A is the yield stress σ_Y at or below T_r. The quantities $\dot{\varepsilon}_p^r$ and C are usually measured at or below the reference temperature.

The dynamic stress-strain behavior in compression of tantalum, which was obtained using rectangular specimens (Wei et al., 2003), and SCS specimens (Rittel et al., 2007)is shown in Fig. 8. The results are for relatively small plastic strain where the softening due to temperature is negligible. Using n =0.82 which best fits the quasi-static results (Rittel et al., 2007; Wei et al., 2003) the JC parameters are: $A = 575$ MPa, $B = 75$ MPa and $C = 0.10$. It can be observed in Fig. 8 that the JC model with the above-mentioned parameters fits well the experimental results for small plastic strains (up to 0.3), without significant thermal softening.

We try to fit the JC model to much higher plastic strains for which both the strain rate effect and the temperature effect are influential, and can no longer be neglected. We assume that the obtained parameters for small plastic strain A, B and n for $\dot{\varepsilon}_p^r = 1000$ 1/s are still valid and we search for C and m that minimize

$$\min \left\{ \sigma_{eq}^* - \left[A + B(\varepsilon_p)^n\right] \left[1 + C \log\left(\frac{\dot{\varepsilon}_p}{\dot{\varepsilon}_p^r}\right)\right] [1 - \Theta^m]\right\}^2 \qquad (5)$$

The $\sigma_{eq}^*(\varepsilon_p)$ is the experimental equivalent Mises stress shown in Fig 6a. The strain rate $\dot{\varepsilon}_p(\varepsilon_p)$ and the temperature $T(\varepsilon_p)$ are shown in Fig. 7. A minimum for the $0 < \varepsilon_p < 0.5$ was found by keeping $C = 0.10$ and setting $m = 0.8$. We assume that damage initiates at $\varepsilon_p = 0.5$, and that is the reason for the change of slope observed in Fig. 4.

2.2.3. Validation of the JC model and application of damage evolution

A numerical validation process is applied to the obtained JC material model. The process is identical to the process detailed in Section 2.2.1. The purpose of this validation was to check if the experimental results $\Delta u - f_{out}$ can be replicated with the use of the JC material parameters, and eventually update them until it does so.

Fig. 9 shows a comparison between the experimental $\Delta u - f_{out}$ to the numerically obtained $\Delta u - f_{out}$. It can be observed that the JC model predicts the force very well up to an applied displacement of ~1.2 mm. The latter corresponds to an average plastic strain in the gauge of ~0.6 (Eq.1). For higher plastic strain, the JC model overestimates the applied load. It means that for larger plastic strain, there is more softening than what the JC model predicts.

To model softening, a ductile failure with tabular damage evolution variable (d^*) (Simulia, 2014b) is added to the JC model. The damage evolution variable is based on the effective plastic displacement $\widehat{u}_p$: $d^* = d^*(\widehat{u}_p)$ where $\dot{\widehat{u}}_p = L \dot{\varepsilon}_p$ with L being the characteristic length of the element. Using a trial and error process, we could better fit numerically the experimental $\Delta U - f_{out}$ by using the tabular damage of Table 5. The numerically obtained $\Delta U - f_{out}$ (red line) is in good agreement with the experimental one (black line). The good agreement for the applied force confers reliability to the obtained JC material model with the ductile failure and damage evolution which is summarized in Tables 3-5.
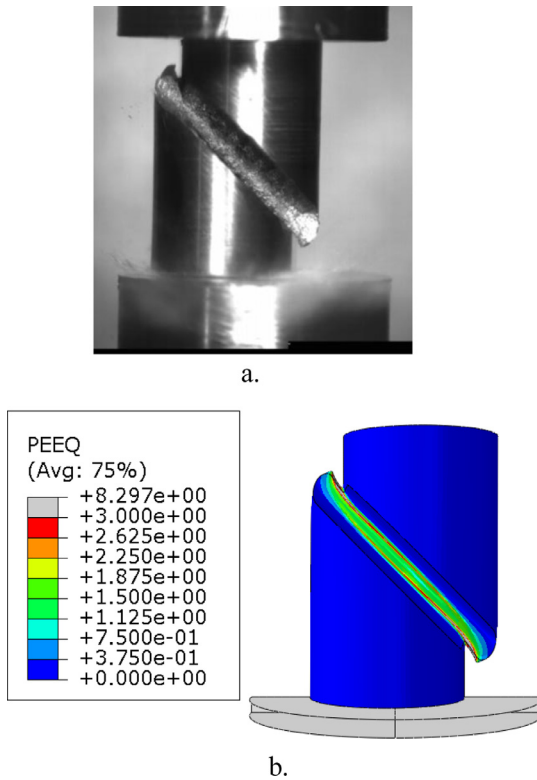
The tantalum SCS specimen at applied displacement ΔU of ~3 mm is shown in Fig. 10. Fig. 10a shows a picture taken by a fast camera (Kirana). Fig. 10b shows the numerical simulation result using the obtained JC material model. The experimental and numerical deformation patterns match very well.
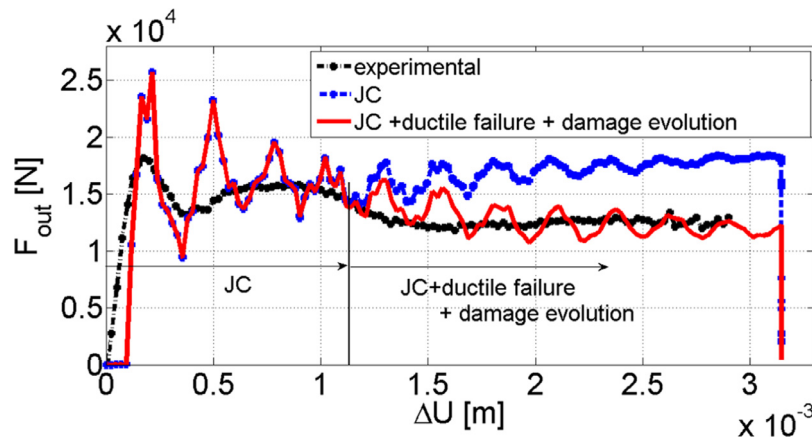
Fig. 9. Comparison between experimental results and numerically calculated $\Delta U - f_{out}$ using the JC material model with and without ductile failure and damage evolution.

Table 5
Damage versus the effective plastic displacement.

Damage initiation $\varepsilon_p^* = 0.6$	$\bar{u}_p$ [μm]	0	50	2000	4000
	Damage	0.0	0.3	0.34	0.38

a.

b.

Fig. 10. Tantalum specimens at applied displacement ΔU of ~3 mm. a. A picture taken by a fast camera. b. The numerical simulation result using JC material model with ductile failure and damage evolution.

3. Dynamic properties of tantalum in shear-tension

3.1. Experimental results

Three shear tension specimens (STS) specimen, which their geometry shown in Fig. 11 were tested in a split Hopkinson tension bars apparatus (SHTB), made of hardened C300 maraging steel tension bars. The geometry of the specimens is similar to the quasi-static specimens (Fig. 1) with $L = 30$ mm and $D = 12$ mm. The specimen is screwed on both sides to the bars using 5/16 UNF threads with 10 mm length.

The recorded pulses during the three tests are shown in Fig. 12a. The high degree of repeatability of the experiments is noticeable. The recorded pulses are used to calculate the applied forces on both side of specimen. These forces are plotted in Fig. 12b where F_{in} is on face perpendicular to the incident pulse bar and F_{out} is on a face perpendicular to the transmitted pulse bar. It can be observed that during the early stage of the pulse (50–60 μs), there is no dynamic force equilibrium; hence properties obtained in this time regime are not accurate.

3.2. Numerical –experimental results

The dynamic flow behavior and ductility of the STS is obtained by hybrid numerical-experimental technique using "trial and error" procedure (Dorogoy et al., 2016). We use the dynamic properties obtained by the SCS as a first guess. We modify the failure strain
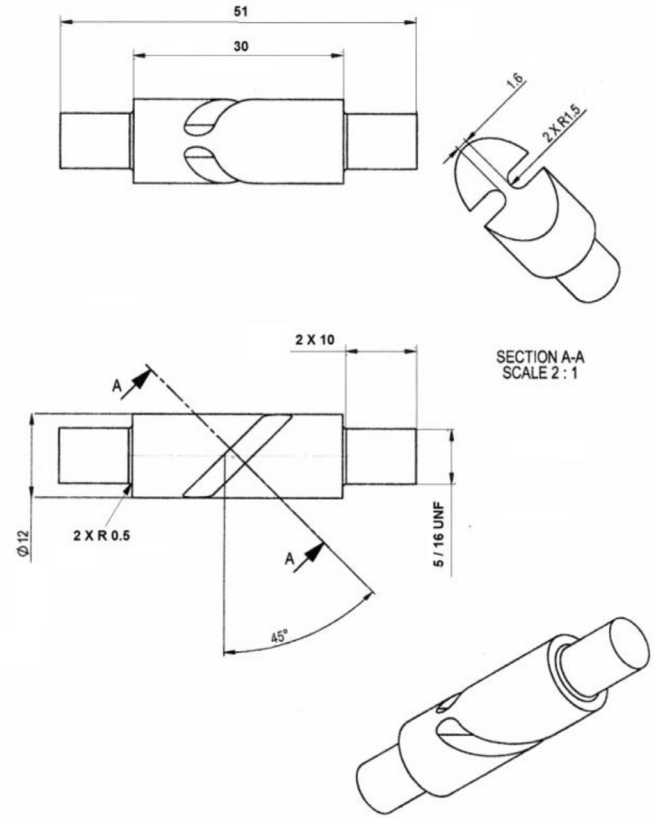
Fig. 11. Shear Tension Specimen (STS) for dynamic tension.

a.

b.
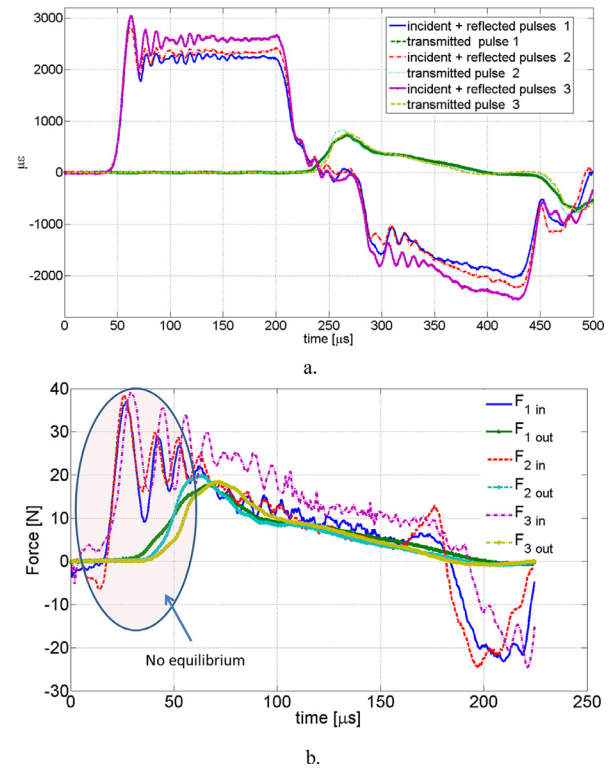
Fig. 12. Experimental results. a. The recorded strain pulses. b. The experimentally measured forces on both side of the specimen. Note that there is no equilibrium in the first 50 μs until the F_{out} reaches its maximum value.
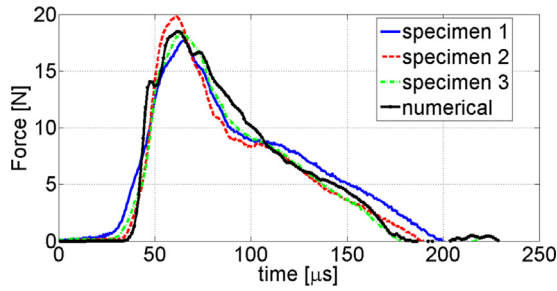
Fig. 13. Comparison of the numerically obtained $F_{out}(t)$ to the experimental measured ones.
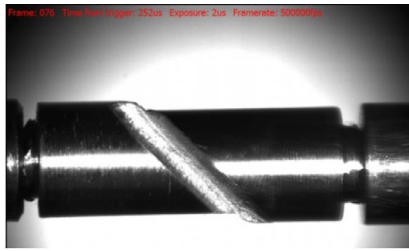
Table 6
JC parameters for tantalum in shear-tension for strain rates of $10^3 – 10^4$ 1/s.

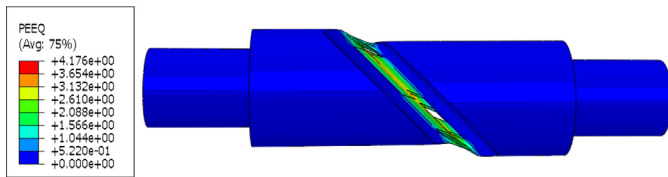| A [MPa]	B [MPa]	n	C	m	Tr [C°]	Tm [C°]	$\dot{\varepsilon}_p^r$
625	75	0.82	0.10	0.8	25	2975	1000

Table 7
Damage versus the effective plastic displacement in shear tension.

$\varepsilon_p^f = 0.15$	$\bar{u}_p$ [µm]	0	100	200	430	800
	Damage	0.0	0.3	0.3	0.6	1.0

a.

b.

Fig. 14. The STS at onset of fracture. a. A picture taken by a fast camera (Kirana). b. Numerical simulation with equivalent plastic strain distribution.

and the damage evolution until there is a good agreement between the dynamic experimental measured applied force and numerically calculated applied force (F_{out}).

Fig. 13 shows the converged numerical $F_{out}(t)$ in comparison to three experimental curves . This good agreement was achieved using the JC material properties of Table 6 together with damage properties of Table 7. There is only one difference in the JC properties between shear-compression (Table 3) and shear-tension (Table 6): A = 575 MPa for shear-compression and A = 625 MPa for shear-tension. This difference can be attributed to the different Lode parameter in both types of loading.

The STS at onset of fracture is shown on Fig. 14a. This picture was taken by a fast camera (Kirana) at 252 μs from trigger. Fig. 14b shows the specimen and plastic strain distribution (PEEQ) at the same time from trigger. Similar pattern of deformation can be observed and fracture occur ate the same time.
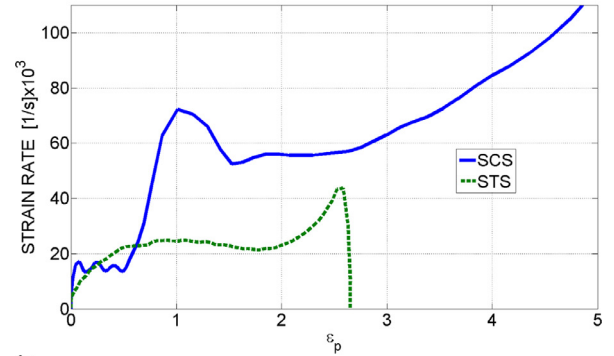
4. Comparison between dynamic results of SCS and STS

The evolution of Mises stress versus the equivalent plastic strain on the centroid of single elements located at the mid gauge of the STS and SCS is shown in Fig. 15a. Both specimens experience very high plastic deformations and the damage behavior of tantalum is shown. While the STS has fractured at plastic strain of ~2.6 the SCS could carry much larger plastic strains. The ductility (fracture strain) of the SCS was not reached. The damage initiation of the STS is at $\varepsilon_p = 0.15$ while for the SCS $\varepsilon_p = 0.5$. The damage accumulation in shear-tension is markedly different from shear-compression.
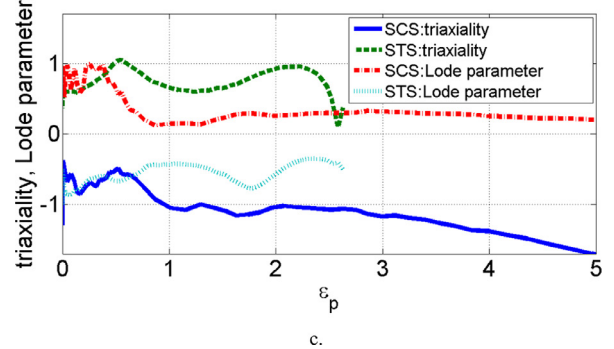
The strain rate of each element of the STS and SCS is shown in Fig. 15c. For small plastic strain, $\varepsilon_p < 0.5$, it is ~20,000 1/s . For larger plastic strains more plastic work is converted to heat hence the temperature rise. This rise of temperature cause softening which together with the damage accumulation lead to more plasticity and higher temperature and strain rate. It can be observed that the element of the STS reaches it peak strain rate just before failure.

a.
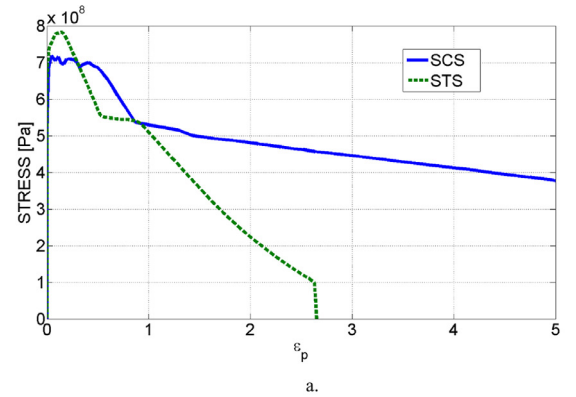
c.

Fig. 15. The evolution of Mises stress, strain rate, triaxiality and Lode parameter versus the equivalent plastic strain (ε_p) on the centroid of single elements located at the mid gauge of the STS and SCS. a. Mises stress. B. strain rate. c. Triaxiality and Lode parameter.

The evolution of the triaxiality and Lode parameter within the examined elements are shown in Fig. 15c. The triaxiality of the SCS is $\sim$−0.5 at $\varepsilon_p = 0.0$ and reaches $\sim$−1 at $\varepsilon_p = 1.0$. For larger plastic strains, the negative triaxiality increases. The triaxiality of the STS is $\sim$0.5 at $\varepsilon_p = 0.0$, and reaches $\sim$1 at $\varepsilon_p = 0.5$. It remains between 0.5–1 up to fracture. The triaxiality is probably the reason for the large difference in the damage behavior of the Tantalum in shear-tension and shear-compression. The triaxiality is known to affect the ductility of metals (Bai et al., 2009). The Lode parameter of the STS is −0.8 at $\varepsilon_p = 0$, and remains rather constant between −0.4 – −0.8.

The Lode parameter of the Ta SCS is $\sim$0.8 at $\varepsilon_p = 0$ and reaches a maximum of 1 at $\varepsilon_p = 0.5$ when damage initiates. During damage accumulation the Lode parameter drops to $\sim$0.2 at $\varepsilon_p = 1.0$ until final failure. This fact indicates that for large strains ($\varepsilon_p > 1.0$) the load changes to from unidirectional compression to a more like general shear loading.

5. Summary and conclusions

The dynamic large strain behavior of polycrystalline tantalum has been characterized using shear-compression and shear-tension experiments over a wide range of high strain rates (103–104 1/s). The modified SCS (shear-compression specimen) and the STS (shear-tension specimen) were utilized for this investigation. The inelastic behavior was described by the Johnson–Cook material model together with ductile failure and damage evolution. The results reveal that the material dynamic failure behavior at high strain rates in shear-tension is markedly different from that in shear-compression. The material was characterized up to very large equivalent plastic strains, which were higher than 5 for the SCS and 2.5 for the STS where fracture occurred. The rate of damage accumulation is more moderate, and hence ductility is higher for shear-compression specimen. During the damage accumulation phase, the triaxiality in the STS is 0.7 – 1 while in the SCS it ranges from −0.5 to −2.0. It is probably the triaxiality which affects the ductility and the rate of damage accumulation in both specimens.

Ackowledgment

Appendix A. Data reduction technique for SCS

A 3D quasi-static nonlinear analysis with Abaqus Standard (Simulia, 2014a) is done to determining the relations between the applied load (P) and displacement (d) to the average strain ($\widehat{\varepsilon}_p$) and stress ($\widehat{\sigma}$) on the gauge mid cut section using the general formulation:

$$\widehat{\varepsilon}_p = f\left(\frac{d - d_y}{h}\right) \tag{A1}$$

$$\widehat{\sigma} = g(\widehat{\varepsilon}_p)\frac{P}{Dt} \tag{A2}$$

where d is the applied displacement and d_y (Fig. 6a) is the displacement at which the mid cut section of the gauge starts to yield. The height of the gauge is h. The applied load is P. The geometrical parameters D and t are the diameter of the specimen and the gauge thickness, respectively. The functions f and g are determined from the numerical analysis. The Tantalum SCS specimen is shown of Fig. 1.
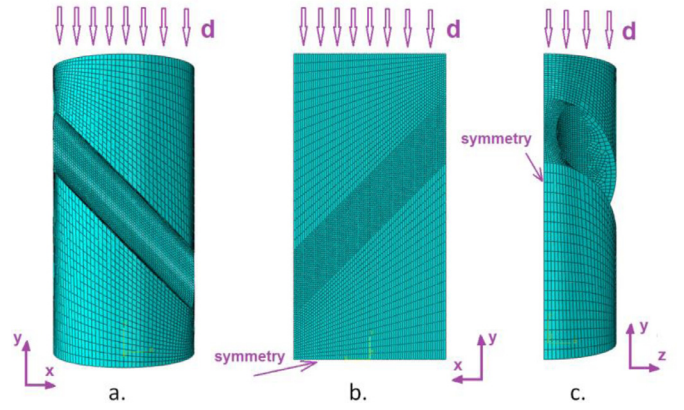

Fig. A1. The meshed SCS model showing the applied boundary conditions. a. Front view b. Back view. c. Side view.

Mesh and boundary conditions

Because of symmetry, only one-half of the specimen was modeled as shown in Fig. A1 Symmetry conditions in the z direction were applied along the symmetry cut (Fig. A1c). Symmetry conditions on the y direction were applied on the bottom (Fig. A1b). The center point on the bottom was fixed. A vertical downward displacement of 3 mm was applied on the upper face.

The mesh of the model which is shown in Fig. A1 consists of 79,300 linear hexahedral elements of type C3D8 having an edge seed size of 0.2 mm within the gauge region.

Material properties and analysis

An elastic-plastic material model was used for the Tantalum (Ta). The Young's modulus: E = 186 GPa and Poisson's ratio of 0.35. The yield stress was taken as 920 MPa and a very small hardening was assumed as shown in Fig. A2b. These properties are for strain rate of 6000–7000 1/s (Wei et al., 2003).

Results and data reduction

The mid cut section is of the gauge is shown in Fig. A2a. The average Mises stress versus the average plastic strain on the mid-cut section of the gauge is plotted in Fig A2b together with the material property input curve to Abaqus. **It can be observed that the average values on the mid cut section replicate the material property**. This fact was shown in previous studies (Dorogoy et al., 2015; Dorogoy and Rittel, 2006).

Fig. A3a shows the average plastic strain on the mid cut section versus the applied displacement.

From this non-linear relation the function f can be obtained:

$$\widehat{\varepsilon}_p = k_{31}\frac{d - d_y}{h} + k_{32}\left(\frac{d - d_y}{h}\right)^2 + k_{33}\left(\frac{d - d_y}{h}\right)^3 \tag{A3}$$

Where $k_{31} = 4.35$, $k_{32} = -5.886$ and $k_{33} = 3.47$.

Fig. A3b shows the average values of the Mises stress and the applied stress $\frac{P}{Dt}$ versus the plastic strain on the mid cut section of the gauge. From the ratio between these two curves, which is shown in Fig. A4, the function g is obtained:

$$g(\widehat{\varepsilon}_p) = p_5\varepsilon_p^4 + p_4\varepsilon_p^3 + p_3\varepsilon_p^2 + p_2\varepsilon_p + p_1 \tag{A4}$$
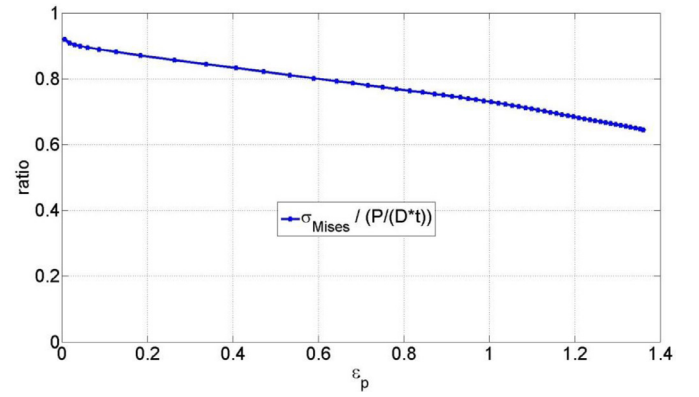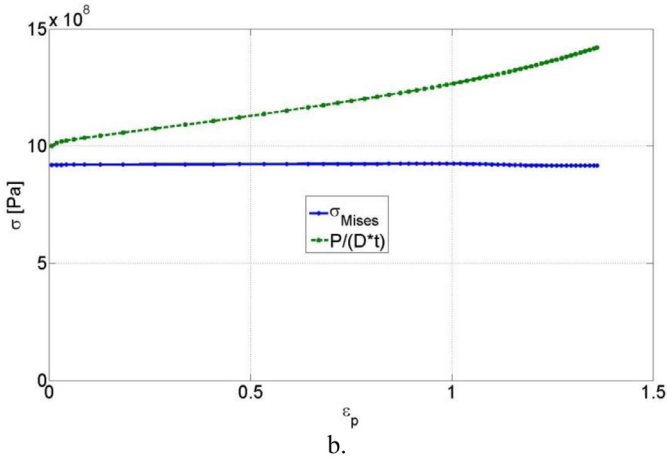
Where $p_1 = 0.9133$, $p_2 = -0.2676$, p3 $= 0.2337$, $p_4 = -0.195$ and $p_5 = 0.04498$.

Eqs. (A1–A4) serve to reduce the measured experimental load-displacements (d-P) curves into the material property curve ($\widehat{\sigma} - \widehat{\varepsilon}_p$), where $\widehat{\sigma}$ is the true stress and $\widehat{\varepsilon}_p$ is the Von Mises equivalent plastic strain.
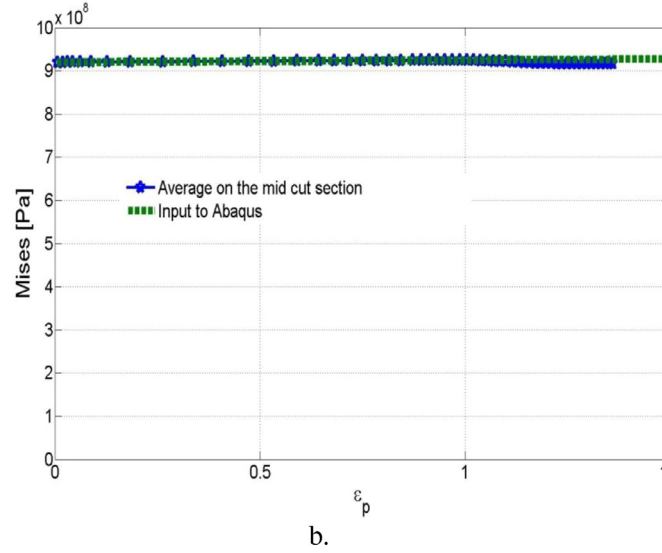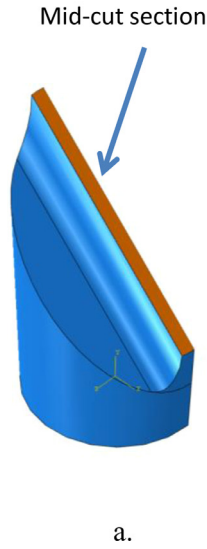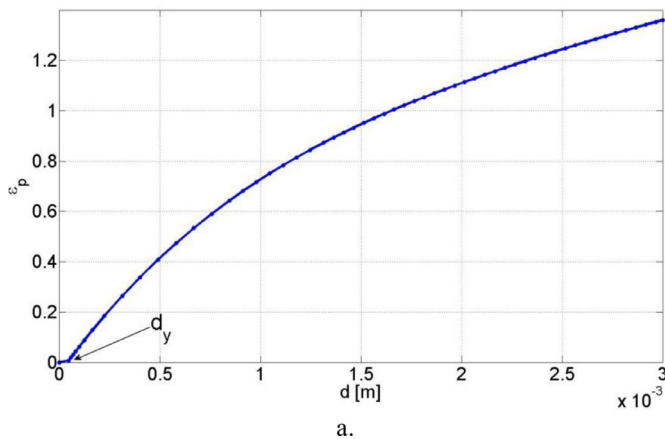
Fig. A2. a. The mid cut section of the gauge. b. The average Mises stress versus the average plastic strain on the mid-cut section in comparison to the material property input Abaqus.

Fig. A4. $\widehat{\varepsilon}_p$ of Eq. (4).

Table B1
Material properties.

	Steel 1020	C300 Managing steel
density ρ $\frac{Kg}{m^3}$	16690	8000
Young's modulus E GPa	186	184
Poison's ratio ν	0.35	0.3
c m/s	3338	4800

Fig. A3. a. The average plastic strain on the mid cut section versus the applied displacement. b. The average Mises stress versus the average plastic strain on the mid-cut section in comparison and the applied stress P/ (D t) versus the average plastic strain on the mid-cut section.

Appendix B. STS Numerical model

The numerical model included three parts: 1) half of the incident bar. 2) The SCS specimen. 3) The transmitted bar. The assembly of these parts is shown in Fig. B1a. A magnified region of the STS specimen is shown in Fig. B1b. The front view on top of Fig B1b and the cut back view on the bottom of B1b. It was assumed in the analysis that the STS specimen is perfectly bonded to the incident and transmitted bars. The bonded area can be seen in the cut view. Because of symmetry, only half of the three merged parts were modeled.

The model uses a total number of 136,792 linear hexahedral elements. 19,502 linear hexahedral elements of type C3D8 were used on the specimen and gauge. All other elements were C3D8R having reduced integration. The mesh size in the SCS gauge region is ~0.3–0.5 mm. Symmetry conditions were applied all along the assembly on the face shown in Fig. B1b.

An elastic material model was used for the SHPB bars (Table B1). An elastic-plastic material model was used for the Tantalum
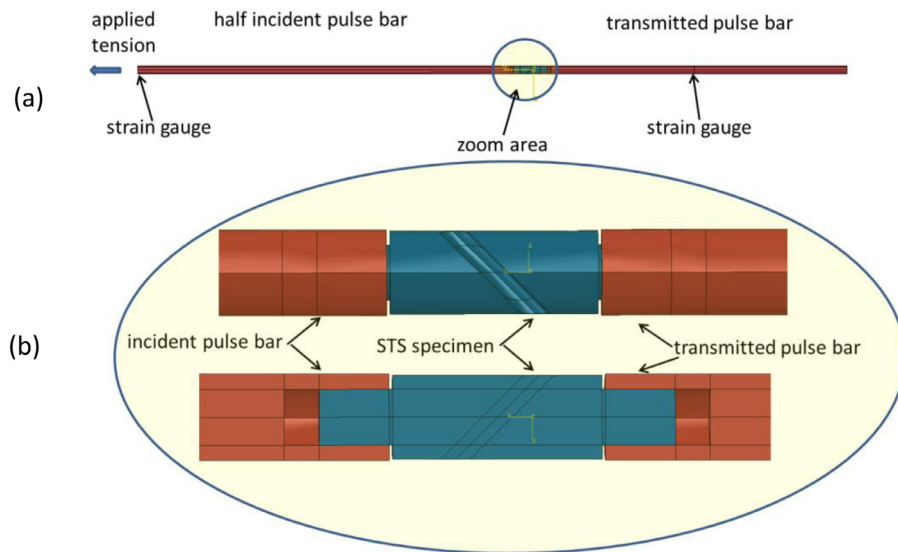
Fig. B1. The model assembly that was used for the numerical validation. a. The assembly. b. Magnification of the specimen area showing the connection to the bars.
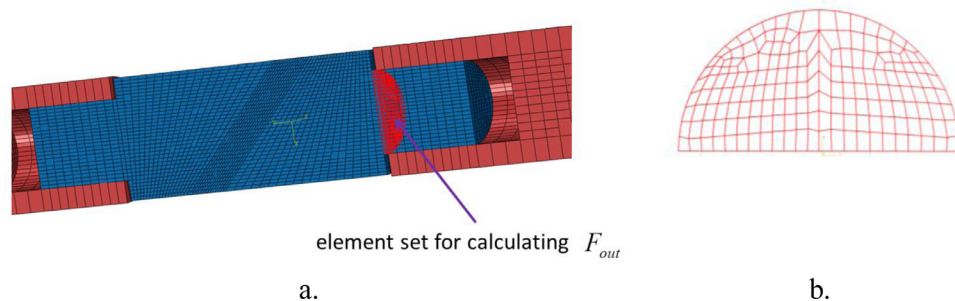
Fig. B2. a. The location of the "free body cut" for calculation of F_{out}. b. The elements shape on the face on which F_{out} is calculated.

specimen. The JC plasticity was used with the parameters obtained by the dynamic testing of SCS. The purpose of the analyses is to obtain the failure strain with its associated damage evolution by a trial and error process.

The load was applied at the left end of the half incident bar. At that location in the experimental setup, a strain gauge is used to measure the incident and reflected pulses. The measured incident strain pulse multiplied by the Young's modulus of the bars was applied as a negative pressure. The transmitted pulse is determined at the location (Fig. B1a) of the strain gauge on the transmitted pulse bar. We have checked the value of F_{out} by using Abaqus option: "free body cut". Fig. B2a shows the location of the cut while Fig. B2b shows the elements On which the force was integrated.

References

Bai, Y., Teng, X., Wierzbicki, T., 2009. On the application of stress triaxiality formula for plane strain fracture testing. J. Eng. Mater. Technol. 131 (2), 021002.

Bai, Y., Wierzbicki, T., 2008. A new model of metal plasticity and fracture with pressure and Lode dependence. Int. J. Plast 24 (6), 1071–1096.

Barsoum, I., Faleskog, J., 2007a. Rupture mechanisms in combined tension and shear—Experiments. Int. J. Solids Struct. 44, 1768–1786. doi:10.1016/j.ijsolstr.2006.09.031.

Barsoum, I., Faleskog, J., 2007b. Rupture mechanisms in combined tension and shear—Micromechanics. Int. J. Solids Struct. 44, 5481–5498. doi:10.1016/j.ijsolstr.2007.01.010.

Bhattacharyya, A., Rittel, D., Ravichandran, G., 2007. Strain rate dependency on deformation texture for pure polycrystalline tantalum. Int. J. Mater. Res. 98 (9), 889–893.

Chen, S.R., Gray, G.T., 1996. Constitutive behavior of tantalum and tantalum–tungsten alloys. Metall. Mater. Trans. A 27 (10), 2994–3006.

Dorogoy, A., Rittel, D., 2009. Determination of the Johnson–Cook material parameters using the SCS specimen. Exp. Mech. 49 (6), 881–885.

Dorogoy, A., Rittel, D., 2006. A numerical study of the applicability of the shear compression specimen to parabolic hardening materials. Exp. Mech. 46 (3), 355–366.

Dorogoy, A., Rittel, D., Godinger, A., 2016. A shear-tension specimen for large strain testing. Exp. Mech. 56 (3), 437–449.

Dorogoy, A., Rittel, D., Godinger, A., 2015. Modification of the shear-compression specimen for large strain testing. Exp. Mech. 55, 1627–1639. doi:10.1007/s11340-015-0057-6.

Duprey, K.E., Clifton, R.J., 1998. Dynamic constitutive response of tantalum at high strain rates. In: AIP Conference Proceedings, vol. 429 (1). AIP, pp. 475–478.

Gao, X., Zhang, T., Hayden, M., Roe, C., 2009. Effects of the stress state on plasticity and ductile failure of an aluminum 5083 alloy. Int. J. Plast. 25 (12), 2366–2382.

Hoge, K.G., Mukherjee, A.K., 1977. The temperature and strain rate dependence of the flow stress of tantalum. J. Mater. Sci. 12 (8), 1666–1672.

Johnson, G.R., Cook, W.H., 1983. A constitutive model and data for metals subjected to large strains, high strain rates and high temperatures. In: Proceedings of the 7th International Symposium on Ballistics, vol. 21 (1). AIP, pp. 541–547.

Keshavarz, A., Ghajar, R., Mirone, G., 2014. A new experimental failure model based on triaxiality factor and Lode angle for X-100 pipeline steel. Int. J. Mech. Sci. 80, 175–182.

Khan, A.S., Liang, R., 1999. Behaviors of three BCC metal over a wide range of strain rates and temperatures: experiments and modeling. Int. J. Plast. 15 (10), 1089–1109.

Kolsky, H., 1949. An investigation of the mechanical properties of materials at very high rates of loading. Proc. Phys. Soc. Sect. B 62 (11), 676–700.

LeBlanc, M.M., Lassila, D.H., 1993. Dynamic tensile testing of sheet material using the split-Hopkinson bar technique. Exp. Tech. 17 (1), 37–42.

Lee, B.J., Vecchio, K.S., Ahzi, S., Schoenfeld, S., 1997. Modeling the mechanical behavior of tantalum. Metall. Mater. Trans. A 28 (1), 113–122.

Nemat-Nasser, S., Isaacs, J.B., 1997. Direct measurement of isothermal flow stress of metals at elevated temperatures and high strain rates with application to Ta and TaW alloys. Acta Mater. 45 (3), 907–919.

Nicholas, T., 1981. Tensile testing of materials at high rates of strain. Exp. Mech. 21 (5), 177–185.

Pan, Z., Li, Y., Wei, Q., 2008. Tensile properties of nanocrystalline tantalum from molecular dynamics simulations. Acta Mater. 56 (14), 3470–3480.

Pivonka, P., Willam, K., 2003. The effect of the third invariant in computational plasticity. Eng. Comput. 20 (5-6), 741–753.

Rittel, D., Bhattacharyya, A., Poon, B., Zhao, J., Ravichandran, G., 2007. Thermomechanical characterization of pure polycrystalline tantalum. Mater. Sci. Eng. A 447 (1), 65–70.

Rittel, D., Lee, S., Ravichandran, G., 2002. A shear-compression specimen for large strain testing. Exp. Mech. 42 (1), 58–64.

Rittel, D., Silva, M.L., Poon, B., Ravichandran, G., 2009. Thermomechanical behavior of single crystalline tantalum in the static and dynamic regime. Mech. Mater. 41 (12), 1323–1329.

Simulia, 2014a. Abaqus/CAE version 6.14-2 (2014). Dassault Systèmes Simulia Corp. Providence, RI, USA.

Simulia, 2014b. Abaqus/Explicit Version 6.14-2. Abaqus Documentation . Dassault Systemes 2014.

Wei, Q., Jiao, T., Mathaudhu, S.N., Ma, E., Hartwig, K.T., Ramesh, K.T., 2003. Microstructure and mechanical properties of tantalum after equal channel angular extrusion (ECAE). Mater. Sci. Eng. A 358 (1), 266–272.